Supplementary Information

In Situ Cascade Steric Stabilization of Poly (ionic liquid) mediated Hexagonal Nickel Hydroxide Morphogenesis for High-Performance Flexible Supercapacitor

Abhishek Narayanan [a], Nagaraj S. Naik [a], Samadhan Kapse[b], Ranjit Thapa[b], R Geetha Balakrishna [a], Chandra Sekhar Rout [a, c] Mahesh Padaki[a]*

[a] *Centre for Nano and Material Sciences, JAIN (Deemed-to-be) University, Kanakapura, Ramanagara, Bangalore 562112, Karnataka, India.*

[b] *Department of Physics, SRM University – AP, Amaravati 522502, Andhra Pradesh, India*

[c] *Department of Chemical Engineering, Chungbuk National University, Cheongju, Chungbuk 28644, Republic of Korea*

1. Experimental Section

1.1. Chemicals.

Following earlier studies, our team synthesized Activated carbon (AC)[1]. 1-Vinylimidazole, 1-Bromo butane, 1,4-Dioxane, Methanol, Ethanol, AIBN-Initiator, $Ni(NO)_3.6H_2O$, Aqueous Ammonia, Acetone, KOH flakes, KBr Powder, Polyvinyl Alcohol (PVA) Were purchased from S.D Fine chemicals, All chemicals were used without further purification. Laboratory-prepared deionized water was used throughout the experiments.

1.2 Synthesis of Ionic Liquids (ILs)

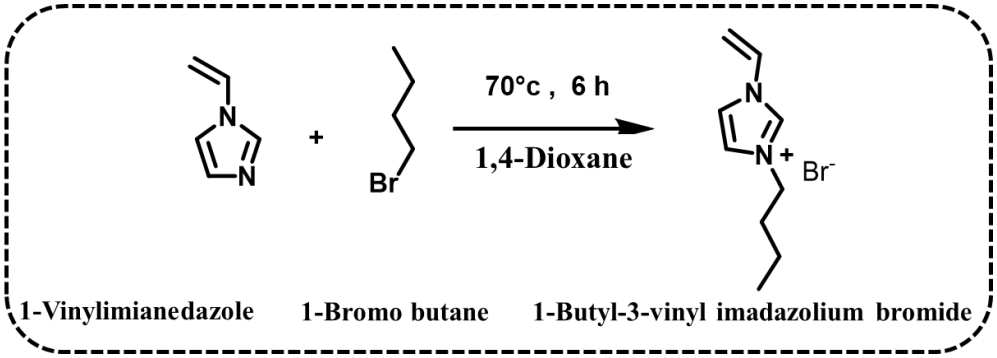

Scheme S1: Synthesis of monomer ((1-butyl-3-vinylimidazolium bromide, ILs)

Firstly, 1-Vinylimidazole (10 g, 0.106 mmol), and 1-Bromo butane (14.559 g, 0.106 mol) were mixed with 1,4-Dioxane (50 mL) as a solvent in a two-necked RB flask which was then degassed under dry nitrogen for 1 hour, filled with nitrogen atmosphere, occupied in an oil bath at 80 ºC for 12 hours, and kept in a reaction under vigorous mechanical stirring. After cooling reaction to RT, the monomer is represented as BVim-Br. The obtained BVim-Br was washed by using 1,4-Dioxane and dried at 80 ºC in a vacuum oven for 24 h to yield a transparent gel-like product was collected. (yield: 85 %).

1.3 Synthesis of poly(ionic liquid)s (PILs)

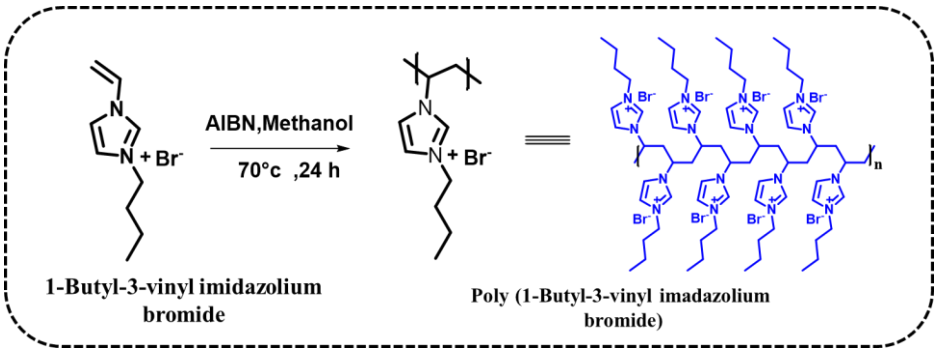

Scheme S2: Synthesis of poly(ionic liquid)s (poly(1-butyl-3-vinylimidazolium bromide (poly(ionic liquid)s, PILs)

1.4 Fabrication of Free-standing device:

Asymmetric solid-state supercapacitors with two oppositely charged electrodes were made utilizing the PVA/$BMIMBF_4$ solid-state electrolyte to assess the PIL-Ni-150 as an electrode material. The initial activated carbon (AC) slurry was created by mixing AC and PVDF in a 9:1 ratio with NMP as the solvent, and PIL-Ni-150 acting as the positive electrode. Using a micropipette, the slurry was drop cast onto the nickel foam mesh in a 2 x 1 cm^2 area. Overnight, the prepared electrodes were dried at 60 °C. The created solid-state electrolyte was placed in between the current collectors and pressed. The packed electrodes were used for further study.

2. Characterization and methods

A) NMR Analysis**:** Prepared poly(ionic liquid)s was characterized by using ^1H NMR (Bruker Avance 400 S) spectral technique recorded with DMSO-d_6 as a solvent and tetramethyl silane (TMS) as the standard.

B) Zeta potential: The surface charge of the prepared samples is measured by using a Zeta potential instrument (Anton Paar, Litesizer™ 500), Laser light of wavelength 658 nm from a single frequency laser diode, providing 40 mW.

C) Field Emission-Scanning Electron Microscopy (FE-SEM): The morphological features of the materials were studied by Field-Emission Scanning Electron Microscopy (FE-SEM, Jeol JSM-7100F).1mg of the samples were ultrasonicated using ethanol as a solvent and drop cast on to the silicon wafer and dried. The image was collected with a voltage of 5 KV and 8 KV and a magnification range from 5000 to 80000.

D) Transmission Electron Microscopy (TEM): The internal morphology, SAED pattern, and elemental mapping were done by using TEM analysis (TALOS F200S G2 200 KV, FEG, CMOS Camera 4K x 4K, In Column EDS Detector). Samples were dispersed using ethanol and drop casted on the surface of Cu grid (300 mesh size) and the image was collected 200-5 nm^{-1}.

E) *p*-XRD Analysis: The synthesized PIL-Ni hybrid was subjected to powder X-ray diffraction (*p*-XRD) (Rigaku X-ray diffractometer) with 2θ ranging from 5 to 80°and 3°/min ramping rate. After done the electrochemical performance of the electrode washed with deionized water, dried and directly subjected to sample holder for further XRD study.

F) FT-IR Analysis: The functional groups were identified by Fourier-Transform Infrared Spectroscopy (FTIR) (Beuker Optik GMBH-FT-IR) in the frequency range 4000 to 500 cm^{-1}. The pinch of sample and KBr powder mixed together and grounded using motor pestle and made the pellet by using pellet press machine by 500 Kg/cm^2 bar pressure and dried sample directly subjected to sample holder for further study.

G) BET Analysis: Nitrogen adsorption-desorption isotherms and pore size distribution were analyzed by Brunauer-Emmett-Teller (BET) analyzer (Belsorp-Max, M/s Microtrac BEL, Japan), degassing temperature was 120 °C and the relative pressure range of 0.1 - 1 used to determine the surface area of the prepared materials.

H) Contact Angle Measurement: To investigate the hydrophilicity of the prepared electrode contact angles carried out (TECH Con-Contact angle measurement, Model No: TECH CON-1200, SI. No: TECH CON-1200/25). Here we check the contact angle of bare nickel foam electrode and nickel foam with prepare material (i.e., PIL-Ni), to meet the small drop of water on the surface of the electrode captured.

I) XPS Analysis: Elemental composition, as well as the chemical and electronic state of the atoms within a material, are analyzed using XPS analysis (PHI 5000 Versa Probe II, FEI Inc). Cu (K α) radiation (λ = 1.5406 Å) was used to measure the x-ray diffraction of in the 2θ between 3° and 32 degrees, with a step of 0.01 degrees and a speed of 2 degrees per minute.

J) TGA Analysis: The thermal stability of materials is analyzed by using a TGA instrument. The sample is heated at a controlled rate in an N_2 environment. According to temperature, the substance's weight changes are noted.

K) UV Analysis: The absorption spectra of dispersed PIL-Ni with water collected from Shimadzu UV-1800 UV spectrophotometer using a 10mm quartz cuvette. The absorption data was collected in the near UV range (200-400 nm).

L) Electrode performance study: All the electrochemical analyses were done using Metrohm Auto Lab B.V. The cyclic voltammetry (CV) and galvanostatic charge-discharge (GCD) was recorded in Nova 2.1 software by using 2M KOH aqueous electrolyetes and PVA/$BMIMBF_4$ solid state electrolyte, in a three and two-electrode system. The electrochemical measurements in three electrodes and two electrodes were studied in a voltage range from 0 to 0.5V and 0-1.6V.

M) Computational Study: DFT calculations are performed using the Vienna Ab initio Simulation Package (VASP)[2], employing the plane-wave technique. The Projected Augmented Wave (PAW) method used to describe core electrons. The electron exchange-correlation

interactions are modeled using the Generalized Gradient Approximation (GGA) proposed by Perdew, Burke, and Ernzerhof [3]. A plane-wave kinetic cut off energy of 450 eV is chosen. For electronic self-consistency, an energy convergence criterion of 10^{-6} eV is employed, while a criterion of 10^{-4} eV is used for ionic relaxation. The Brillouin zone sampling was achieved using the Monkhorst-Pack scheme, with a 9x9x1 K-point grid. To prevent interactions between repeating images, a vacuum of 15 Å was applied in the respective directions.

3. Electrochemical measurements

At room temperature, all electrochemical measurements were performed using an Autolab instrument with Nova 2.1 software. A three-electrode setup was used to assess the supercapacitor's maximum voltage window[4]. The electrochemical impedance spectroscopy experiments were carried out at open circuit potential under a sinusoidal signal with a frequency range of 100 kHz to 10 mHz. At a current density of 5 Ag^{-1}, continuous GCD cycles were used to measure the cycling stability. The mass loading of the active material for the three-electrode and two-electrode systems was carefully measured and found to be 2 mg/cm² and 5 mg/cm^2

The capacitance can also be calculated by integration of the CV curves using the equation S1[5]

$$c = \frac{\int I \, dV}{v \, \Delta V} \qquad \text{S1}$$

where I is the discharge current, i.e., the current below the X axis, v is the scan rate, and ΔV is the operating discharge potential range.

By using equation S2, the specific capacitance derived from GCD curves was computed [6].

$$C = \frac{I\Delta \mathrm{t}}{m\Delta \mathrm{V}} \qquad \text{S2}$$

Where m denotes the quantity of the active materials (g), C denotes specific capacitance ($F\ g^{-1}$), I represents current density (A), t measures time and V denotes potential range.

The change in balance for the asymmetric supercapacitor follows the relationship (S2).

$$q^+ = q^- \qquad \text{S3}$$

The mass ratio of active materials (PIL-Ni-150) and AC is determined using equations S3 and S4, where q + is the change stored in the cathode and q- is the anode[7].

$$q = C \times \Delta V \times m \qquad \text{S4}$$

$$\frac{m^+}{m^-} = \frac{(C^- \times \Delta V^-)}{(C^+ \times \Delta V^+)} \qquad \text{S5}$$

Where m (g) is the active material mass of the electrodes, V (V) is the potential window, and C (F g^{-1}) is the specific capacitance.

Equations S6 and S7 are used to compute the energy density[8,9] (E, Wh kg^{-1}) and power density (P, W kg^{-1}).

$$E = \frac{\Delta V \times i \times \Delta t}{m} \qquad \text{S6}$$

$$P = \frac{\Delta V \times i}{m} \qquad \text{S7}$$

where i is the discharge current; V, voltage; t, time in hours; and m, is the mass of the active materials for both electrode materials.

4. DFT Calculation

In supercapacitors, the total interfacial capacitance (IC) consists of two components: the electric double-layer capacitance (EDLC) and the quantum capacitance (C_Q) of the electrode,

$$\frac{1}{\mathrm{IC}} = \frac{1}{\mathrm{EDLC}} + \frac{1}{\mathrm{C_Q}}$$

Within the local potential window of -1 V < $|\Phi_G|$ < 1 V, the interfacial capacitance (IC) is predominantly influenced by the quantum capacitance (C_Q) rather than the electric double-layer capacitance (EDLC) [10–12]. The quantum capacitance (C_Q) plays a crucial role in determining the local charge storage capacity of the electrode material in a supercapacitor. It is defined as the $C_Q = d\sigma/d\Phi_G$, derivative of the excess charge density ($d\sigma$) with respect to the local potential ($d\Phi_G$)[13,14]. The excess charge density is,

$$d\sigma = e\int_{-\infty}^{+\infty} D(E)\,[f(E) - f(E - e\,\phi)]dE \quad (1)$$

where $D(E)$ is the density of state, $f(E)$ is the Fermi-Dirac distribution, E is the relative energy with respect to the Fermi energy and e is the elementary electronic charge. So, the C_Q is,

$$C_Q = e^2\int_{-\infty}^{+\infty} D(E)\,F_T(E - e\,\phi)dE \quad (2)$$

where $F_T(E)$ is thermal broadening function.

5. Characterization

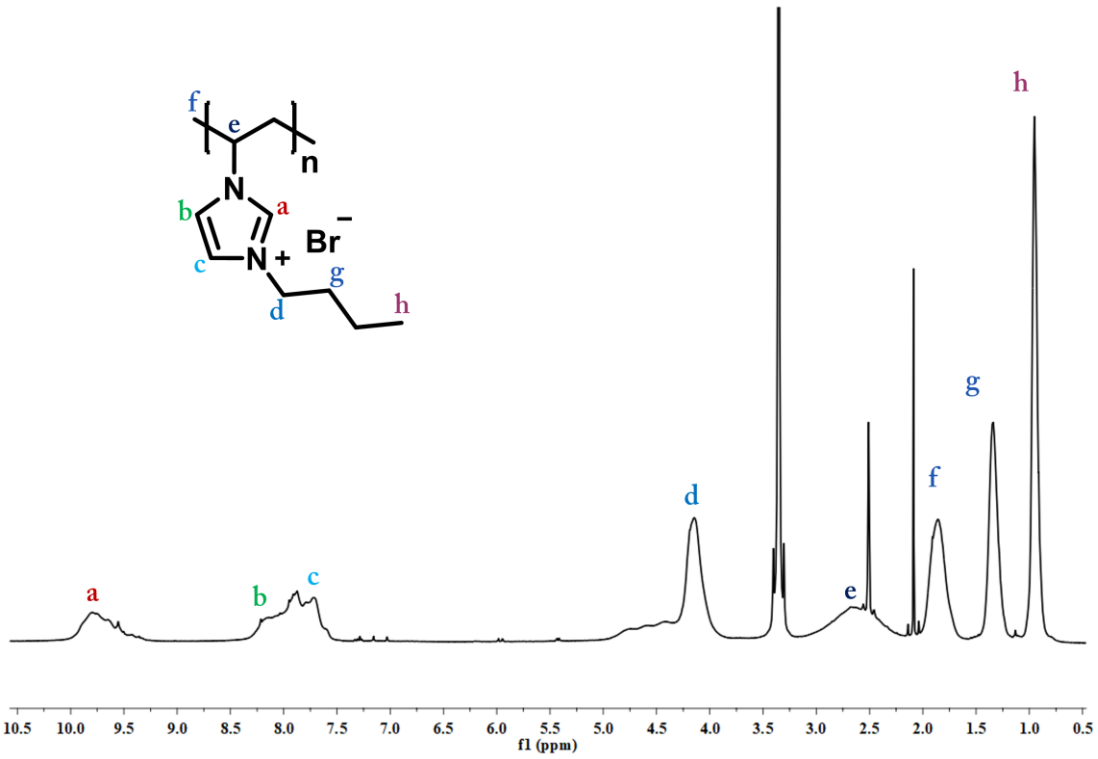

Figure S1: NMR data of poly(1-butyl-3-vinylimidazolium bromide (poly(ionic liquid)s, PIL-Br)

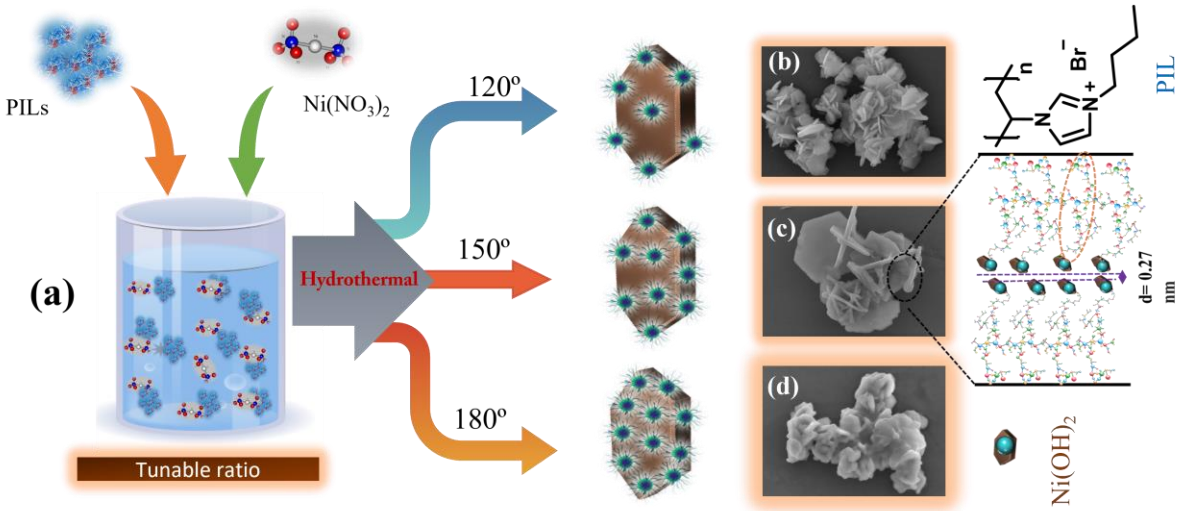

Figure S2: (a) Schematic illustration of formation of hexagonal PIL-Ni-120, PIL-Ni-150 and PIL-Ni-180 crystals, (b)FE-SEM images of PIL-Ni-120, (c)FE-SEM images of PIL-Ni-150 and (c)FE-SEM images of PIL-Ni-180; inset of c showing despacing, structure of poly(ionic liquid) and Nickel hydroxide

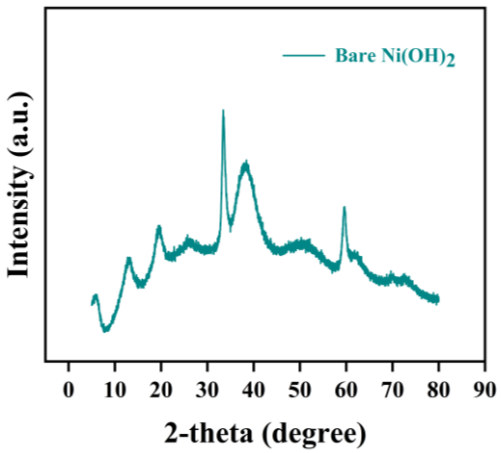

Figure S3: XRD pattern of Bare $Ni(OH)_2$ at 150 °C

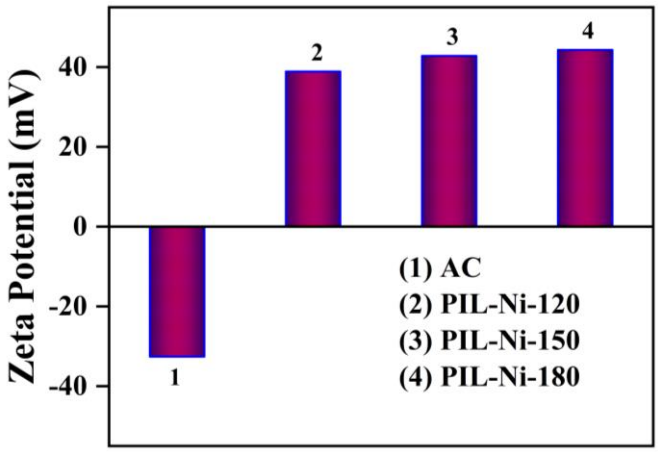

Figure S4: Zeta potential measurement of 1) Activated carbon 2) PIL-Ni-120 3) PIL-Ni-150 and 4) PIL-Ni-180

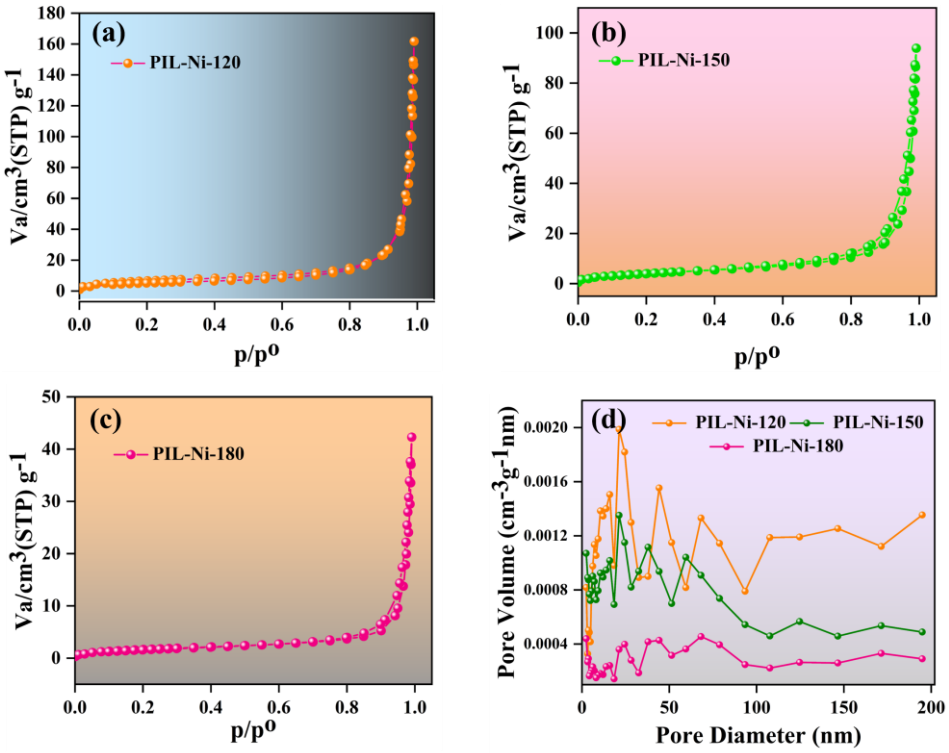

Figure S5: (a-c) N_2 adsorption -desorption isotherms of PIL-Ni-120, PIL-Ni-150 and PIL-Ni-180 and (d) Pore size distribution curve

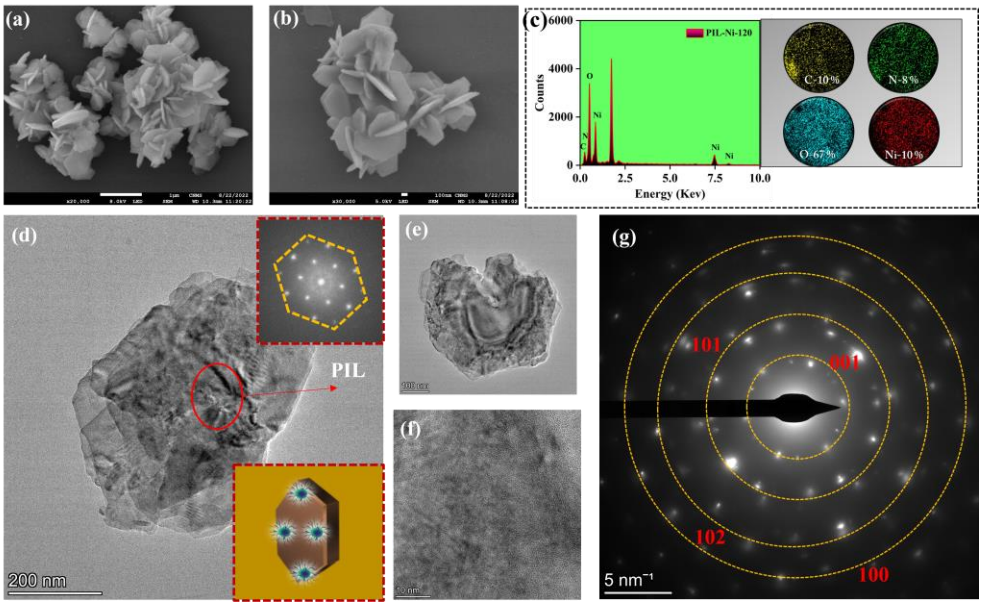

Figure S6: (a) FE-SEM images of PIL-Ni-120 in μm (b) High magnification FE-SEM images of PIL-Ni-120 in nm range (c) Elemental mapping images of PIL-Ni-120 hexagonal nanosheet (d-f) Low and high magnification Transmission electron microscopy images of PIL-Ni-120. Insets of (d, h) confirm the matching SAED patterns and morphological sketch of PIL-Ni-120 (g) SAED pattern of PIL-Ni-120.

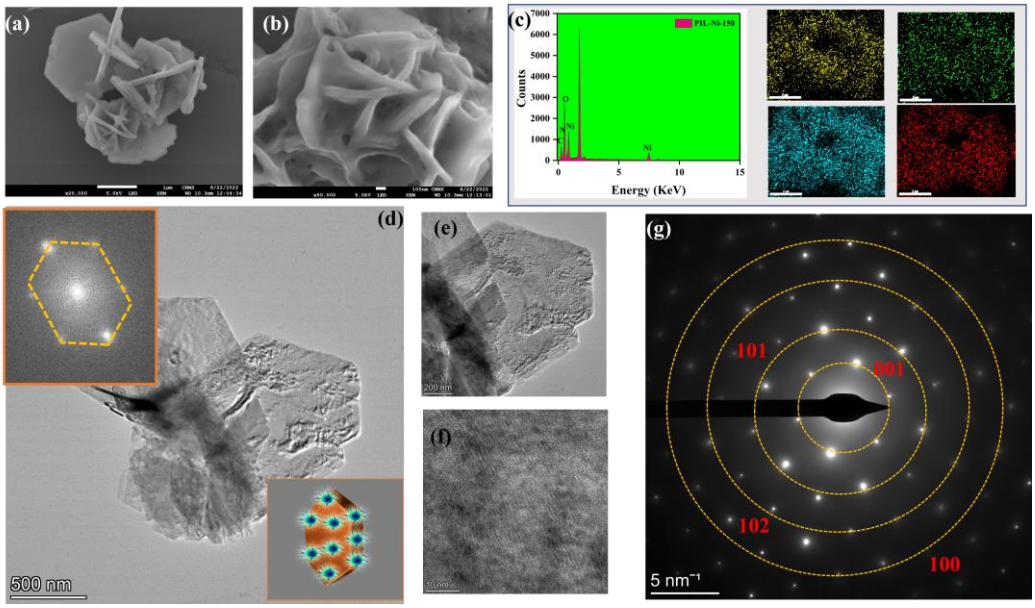

Figure S7: (a) FE-SEM images of PIL-Ni-150 in µm (b) High magnification FE-SEM images of PIL-Ni-150 in nm range (c) Elemental mapping images of PIL-Ni-150 hexagonal nanosheet (d-f) Low and high magnification Transmission electron microscopy images of PIL-Ni-150. Insets of (d, h) confirm the matching SAED patterns and morphological sketch of PIL-Ni-150 (g) SAED pattern of PIL-Ni-150.

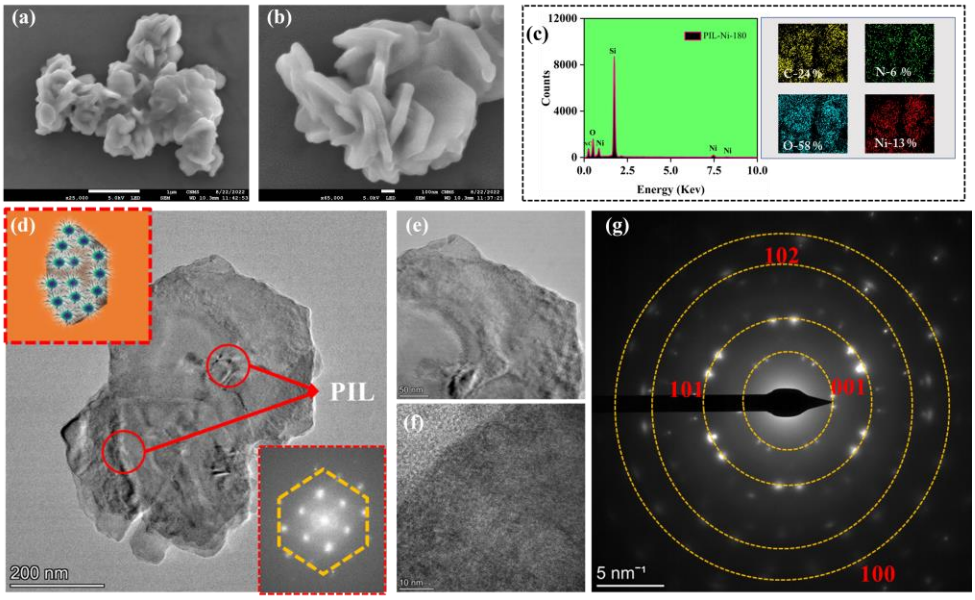

Figure S8: (a) FE-SEM images of PIL-Ni-180 in µm (b) High magnification FE-SEM images of PIL-Ni-180 in nm range (c) Elemental mapping images of PIL-Ni-180 hexagonal nanosheet (d-f) Low and high magnification Transmission electron microscopy images of PIL-Ni-180. Insets of (d, h) confirm the matching SAED patterns and morphological sketch of PIL-Ni-180 (g) SAED pattern of PIL-Ni-180.

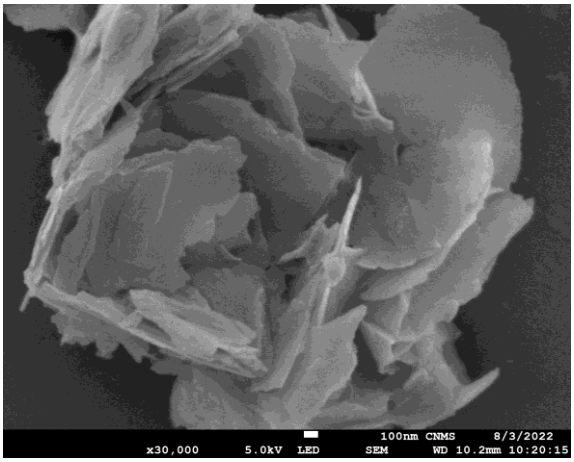

Figure S9: FE-SEM images of Bare $Ni(OH)_2$

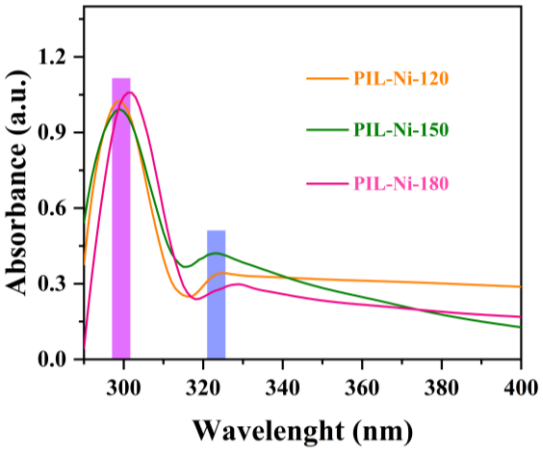

Figure S10: UV analysis data of PIL-Ni-120, PIL-Ni-150 and PIL-Ni-180.

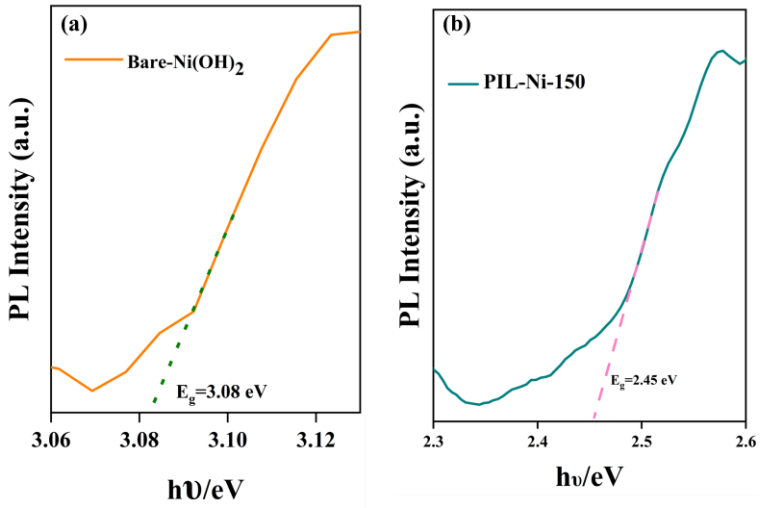

Figure S11: Band gap of PIL-Ni-120, PIL-Ni-150 and PIL-Ni-180 crystals

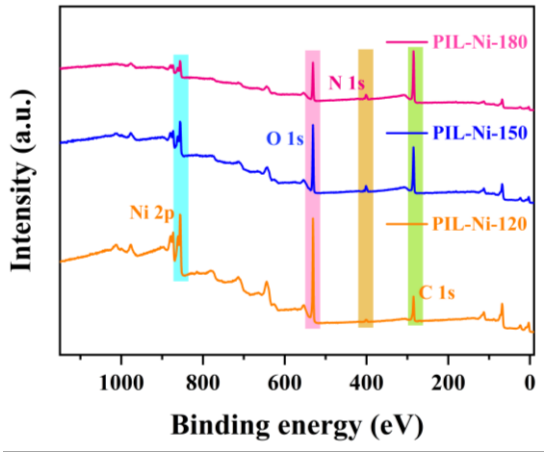

Figure S12: XPS Survey spectra of PIL-Ni-120, PIL-Ni-150 and PIL-Ni-180

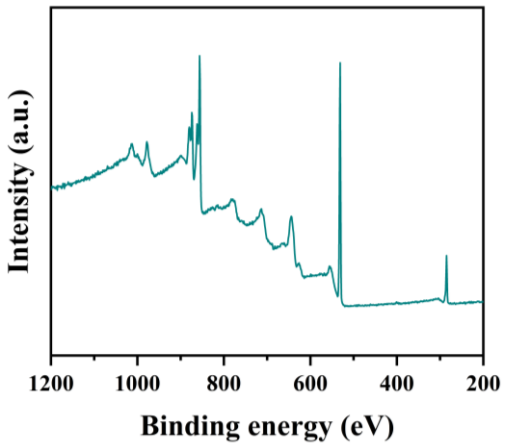

Figure S13: XPS survey spectra of Bare $Ni(OH)_2$

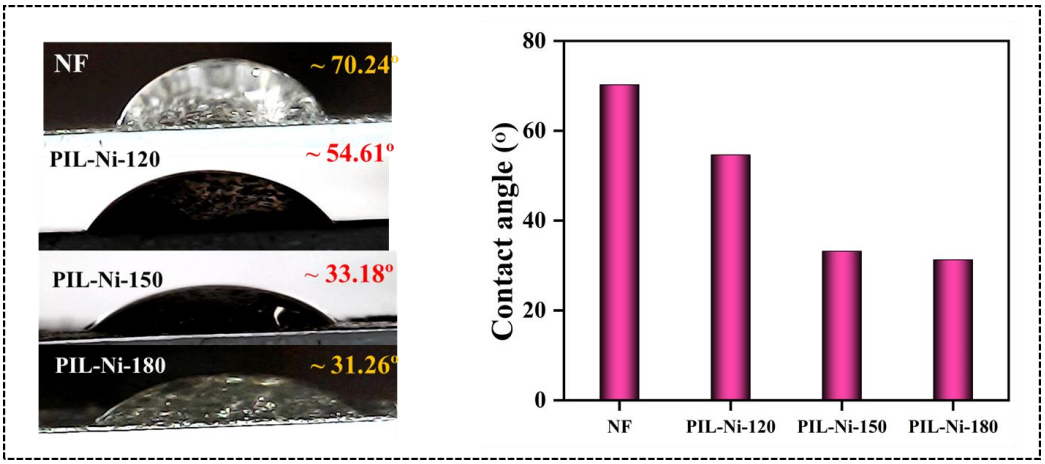

Figure S14: Contact angle measurement of bare nickel foam, PIL-Ni-120, PIL-Ni-150 and PIL-Ni-180.

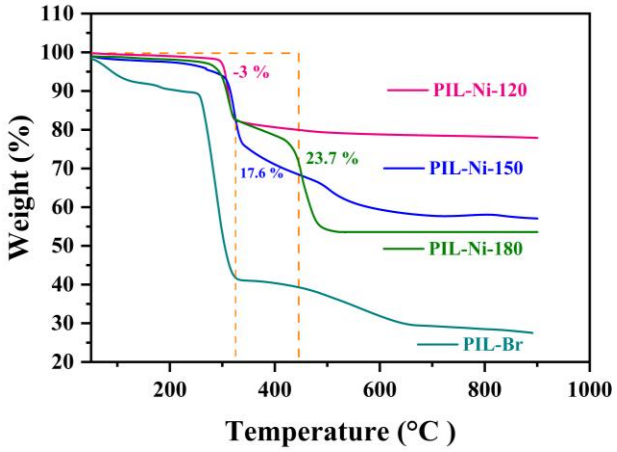

Figure S15: TGA analysis of PIL-Ni-120, PIL-Ni-150 and PIL-Ni-180 compared with PIL-Br

Higher temperatures can significantly accelerate the decomposition of materials. At 180°C, the polyionic liquid (PIL) is likely to undergo more substantial thermal degradation or decomposition compared to 150°C and 120°C, leading to a distinct thermogravimetric (TG) profile. The thermal stability of the PIL varies with temperature. At 180°C, it degrades or reacts differently with $Ni(OH)_2$ than at lower temperatures, causing additional weight loss or producing different decomposition products. Increased temperatures enhance chemical reactions. At 180°C, the interactions between the PIL and $Ni(OH)_2$ intensify, potentially forming new compounds or releasing gases that contribute to weight loss. The structures of both $Ni(OH)_2$ and the PIL may alter at higher temperatures, affecting overall thermal stability and decomposition behavior. These structural changes can lead to variations in the TG curves. At elevated temperatures, the material may follow alternative decomposition pathways, resulting in distinct stages of weight loss that are not observed at lower temperatures.

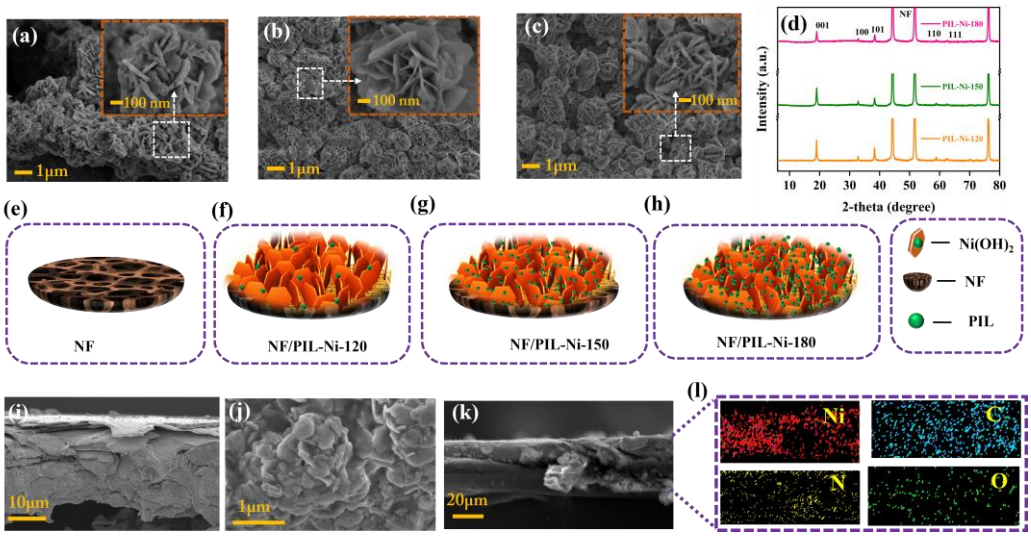

Figure S16: PIL-Ni-120 PIL-Ni-150 and PIL-Ni-180 onto the Nickel foam (a-c) FE-SEM images of PIL-Ni-120, PIL-Ni-150 and PIL-Ni-180 (d) the corresponding XRD pattern (e-f) Schematic representation of hexagonal nanosheet arranged onto the nickel foam (i-k) cross sectional images of PIL-Ni-120 onto the NFs (l) the corresponding elemental maping.

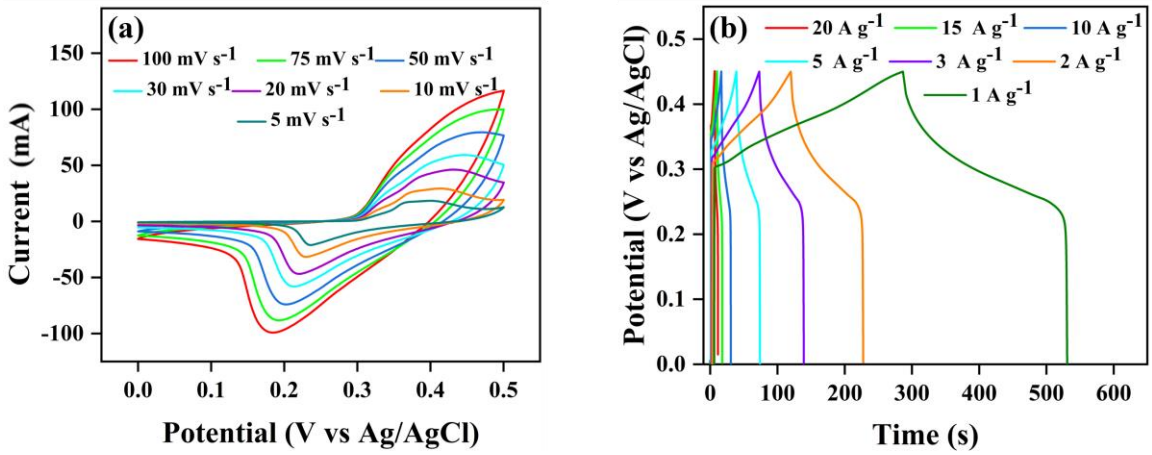

Figure S17: (a, b) CV and GCD of PIL-Ni-120 at different scan rates and current density

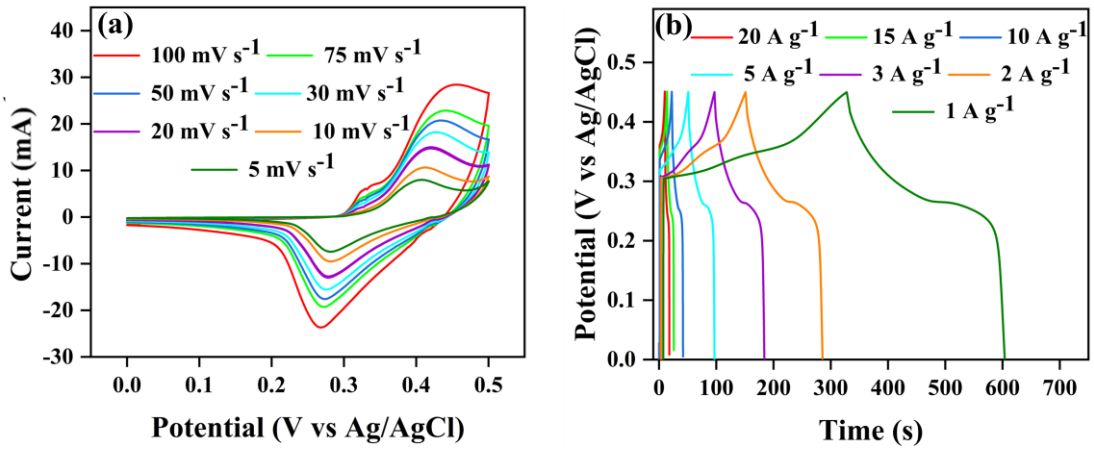

Figure S18: (a,b) CV and GCD of PIL-Ni-180 at different scan rates and current density

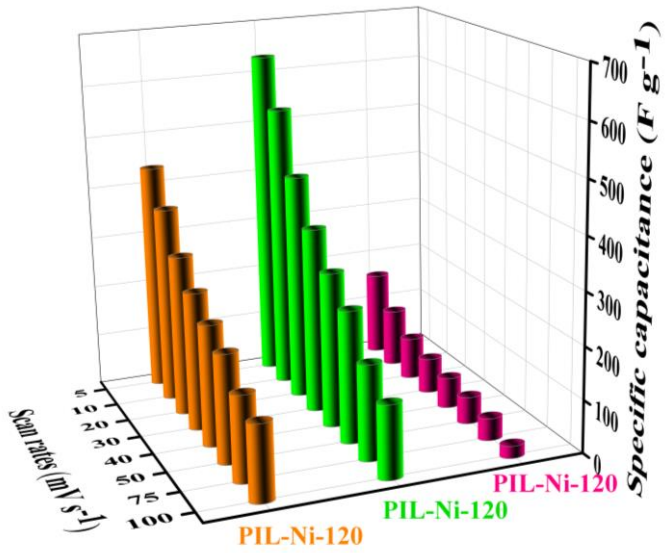

Figure S19: Specific capacitance versus scan rates

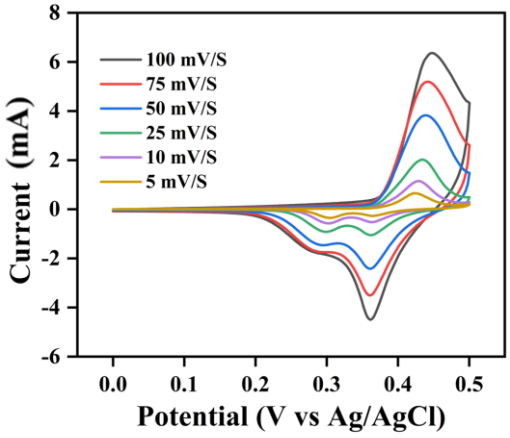

Figure S20: CV of bare NF using 2M KOH electrolyte

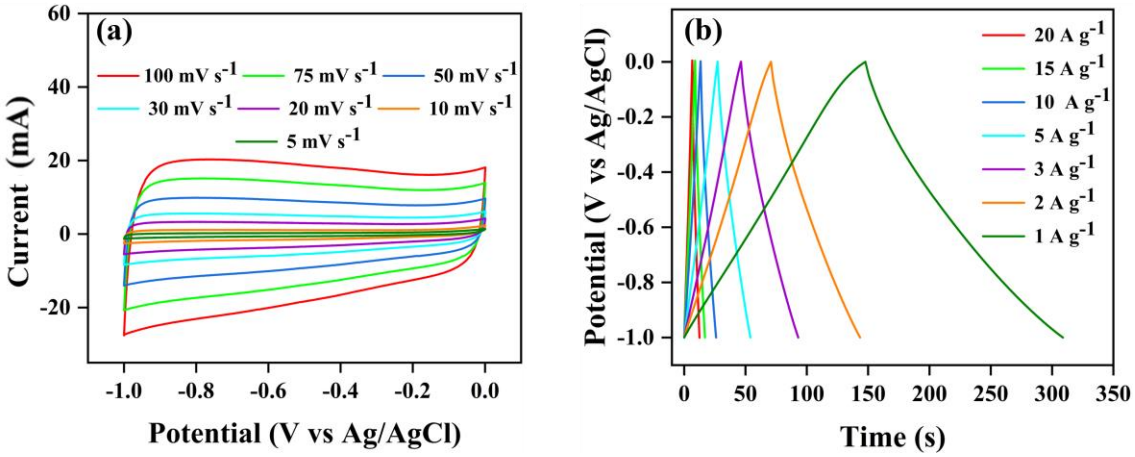

Figure S21: CV and GCD of ACs

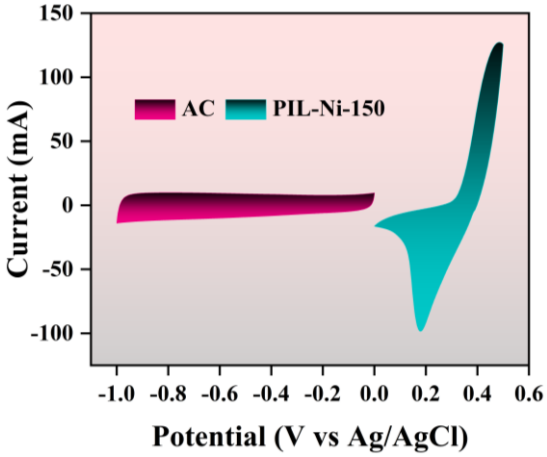

Figure S22: CV of AC//PIL-Ni-120 asymmetric system

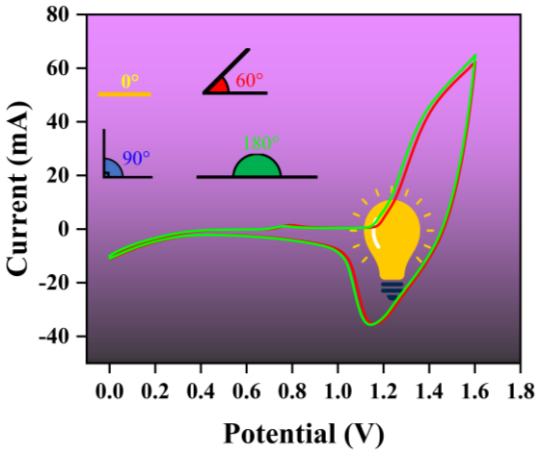

Figure S23: CV of asymmetric SSC at different bending angles

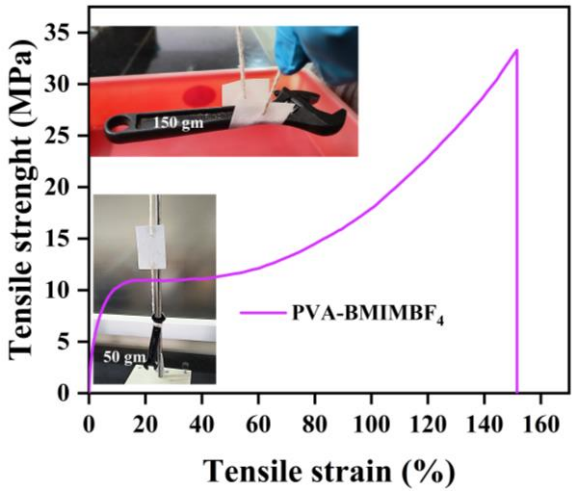

Figure S24: Tensile strength of PVA/$BMIMBF_4$ membrane electrolyte

Table S1: Reliability parameters of PIL-Ni-150

Parameters	**$Ni(OH)_2$**
R_p	37.8
R_{wp}	53.1
R_{exp}	2.64
Go F	20.11
a	3.1259
b	3.1259
c	4.6105
α=β	90
γ	120
Phase	Hexagonal
Volume of the cell	39.017

Table S2: XPS data of PIL-Ni-120, PIL-Ni-150 and PIL-Ni-180

Sample Code	Element	Start BE	Peak BE	Atomic %
PIL-Ni-120	C 1s	298	285.1	32.82
	N 1s	410	400.82	2.82
	O 1s	545	531.01	46.85
	Ni2p	890	855.83	17.51
PIL-Ni-150	C 1s	298	285.06	55.04
	N 1s	410	400.84	6.07
	O 1s	539.03	531.06	30.14
	Ni2p	890	855.58	8.75
PIL-Ni-180	C 1s	298	284.97	69.3
	N 1s	410	400.69	6.06
	O 1s	539.22	531.16	20.05
	Ni2p	890	855.85	4.59

References

1 A. Narayanan, A. Siddiqa, N. K. Kodihalli, G. Hegde, D. H. Nagaraju and M. Padaki, *ACS Sustainable Chemistry and Engineering*, 2023, **11**, 3750–3759.

2 D. Joubert, *Physical Review B - Condensed Matter and Materials Physics*, 1999, **59**, 1758–1775.

3 J. P. Perdew, K. Burke and M. Ernzerhof, *Physical Review Letters*, 1996, **77**, 3865–3868.

4 M. Fu, W. Chen, Y. Lei, H. Yu, Y. Lin and M. Terrones, *Advanced Materials*, , DOI:10.1002/adma.202300940.

5 Y. Shao, M. F. El-Kady, J. Sun, Y. Li, Q. Zhang, M. Zhu, H. Wang, B. Dunn and R. B. Kaner, *Chemical Reviews*, 2018, **118**, 9233–9280.

6 R. Wang, A. Jayakumar, C. Xu and J. M. Lee, *ACS Sustainable Chemistry and Engineering*, 2016, **4**, 3736–3742.

7 X. Chen, S. Wang, G. Qiao, G. Lu, H. Cui and X. Wang, *Energy and Fuels*, 2020, **34**, 16783–16790.

8 J. S. Wei, C. Ding, P. Zhang, H. Ding, X. Q. Niu, Y. Y. Ma, C. Li, Y. G. Wang and H. M. Xiong, *Advanced Materials*, 2019, **31**, 1–7.

9 M. D. S. Michael, K. S. Kesavan and S. R. S. Prabaharan, *Energy Technology*, 2021, **9**, 1–12.

10 R. Samal, M. Bhat, S. Kapse, R. Thapa, D. J. Late and C. Sekhar Rout, *Journal of colloid and interface science*, 2021, **598**, 500–510.

11 M. Mousavi-Khoshdel, E. Targholi and M. J. Momeni, *Journal of Physical Chemistry C*, 2015, **119**, 26290–26295.

12 S. Kapse, B. Benny, P. Mandal and R. Thapa, *Journal of Energy Storage*, 2021, **44**, 103476.

13 W. Zeng, Y. Zhang, X. Liu, L. Qi, W. Kang, L. Fang and M. Zhou, *Applied Surface Science*, 2020, **523**, 146468.

14 I. M. Patil, S. Kapse, H. Parse, R. Thapa, G. Andersson and B. Kakade, *Journal of Power Sources*, 2020, **479**, 229092.